Multi-model attribution of the Southern Hemisphere Hadley cell widening: CMIP3 and CMIP5 models

Seung-Ki Min[1] and Seok-Woo Son[2]

[1]CSIRO Marine and Atmospheric Research, Aspendale, VIC 3195 Australia

[2]Department of Atmospheric and Oceanic Sciences, McGill University, Montreal, QB, Canada

Submitted to JGR-Atmosphere

Corresponding author address: Seung-Ki Min, CSIRO Marine and Atmospheric Research, 107-121 Station Street, Aspendale, VIC 3195, Australia.

E-mail: seung-ki.min@csiro.au

Abstract

It has been suggested that the Hadley cell has been widening during the past three decades in both hemispheres, but attribution of its cause(s) remains challenging. By applying an optimal fingerprinting technique to 7 modern reanalyses and 49 coupled climate models participating in the CMIP3 and CMIP5, here we detect an influence of human-induced stratospheric ozone depletion on the observed expansion of the Hadley cell in the Southern Hemisphere (SH) summer. The detected signal is found to be separable from other external forcings that include greenhouse gases (GHGs), confirming a dominant role of stratospheric ozone in the SH-summer climate change. Our results are largely insensitive to observational and model uncertainties, providing additional evidence for a human contribution to the atmospheric circulation changes.

1. Introduction

Recent observational studies have shown that the tropical belt has been expanding poleward in both hemispheres since the late 1970s [*Seidel et al.*, 2008; *Davis and Rosenlof*, 2012]. While the trends are questionable in quantity, various diagnostics, including the Hadley cell edge, tropopause height, westerly jet, outgoing long-wave radiation, or precipitation minus evaporation [*Davis and Rosenlof*, 2012], show qualitative consensus. Among others, the Hadley cell (HC) edge, derived from zonal-mean mass streamfunction in mid-troposphere, exhibits consistent long-term trends among different reanalyses [*Hu and Fu*, 2007; *Hu et al.*, 2011; *Stachnik and Schumacher*, 2011; *Davis and Rosenlof*, 2012]. The mechanism(s) of the HC widening, however, still remains to be determined.

To identify potential cause(s) of the HC widening, several modelling studies examined the response of HC width to different external forcings including stratospheric ozone depletion, greenhouse gases (GHGs) increase, changes in aerosol loading, and sea surface temperature (SST) changes [*Lu et al.*, 2007, 2009; *Son et al.*, 2009, 2010; *McLandress et al.*, 2011; *Polvani et al.*, 2011b; Ming and Ramaswamy, 2011]. In particular, *Johanson and Fu* [2009] have suggested likely influences from both GHGs and stratospheric ozone changes in annual-mean HC widening through qualitative comparisons with observations. *Lu et al.*[2009] have also attributed the tropical belt expansion to GHGs and ozone by examining tropopause height variability. In regards of relative importance of GHGs increase and stratospheric ozone depletion in the poleward expansion of the SH HC, *McLandress et al.* [2011] and *Polvani et al.* [2011b] proposed a predominant role of stratospheric ozone depletion in the austral summer (December to February, DJF). It is argued that SH-summer HC widening

during the last three decades is largely due to the Antarctic ozone depletion with rather weak contributions by GHGs and SST changes.

Most of previous studies are, however, based on single-model sensitivity test or qualitative comparison of multiple models. To date, no formal attribution studies have been performed, which require direct comparisons between observations and multi-model simulations with rigorous consideration of internal variability. Especially none of the previous studies has separated out the relative contribution of each forcing to the *observed* change in the HC width. In this study, we compare long-term changes in HC width and edges from multiple reanalyses and multiple climate models using an optimal fingerprinting technique. Focusing on austral summer, we separate the influence of stratospheric ozone from other forcings on the observed HC expansion. Among other forcings, GHGs increase is the most likely factor since aerosols and solar and volcanic activities are expected to play only a minor role or even an opposite role in the HC widening [*Lu et al.*, 2009; *Ming and Ramaswamy*, 2011].

2. Data and methods

We compute the HC outer boundary in each hemisphere, which is defined as the latitude where mass stream function at 500 hPa becomes zero. The mass stream function is calculated by integrating density-weighted zonal-mean meridional wind in the vertical from 10 hPa to the surface [*Stachnik and Schumacher*, 2011]. This method has been widely used as a tropical belt diagnostic [*Hu and Fu*, 2007; *Lu et al.*, 2007; *Johanson and Fu*, 2009; *Son et al.*, 2009] and is not affected by threshold selections [*Davis and Rosenlof*, 2012]. The width of the HC is then simply defined as the distance between the southern and northern edges.

For observational analysis we use the ensemble average of seven modern reanalyses (ENM7) that provide data for 30 DJFs between December 1979 to February 2009 (Table 1). We also test the sensitivity of our results to the use of each individual reanalysis as the observation. Multi-model simulation data are obtained from CMIP3 [*Meehl et al.*, 2007] and CMIP5 simulations [*Taylor et al.*, 2012] (Table 2). For extended analysis up to 2009, 20C3M (1979-2000) simulations are combined with A1B runs (2001-2009) from CMIP3 models, which then are divided into two groups of models with and without stratospheric ozone depletion (referred to as OZ3 and noOZ3 respectively). For CMIP5 runs, *historical* experiments (1979-2005) are combined with RCP4.5 runs (2006-2009), all of which include ozone changes (referred to as OZ5). In addition, preindustrial control simulations from 32 CMIP5 models (CTL5) are used to estimate internal variability (see below).

In all analyses, the original horizontal grids are used. Although not shown, analyses using interpolated data onto the same 2.5° latitude by 2.5° longitude grids show essentially the same results, indicating negligible sensitivity to the horizontal resolution. In the vertical, only standard pressure levels from the CMIP3 models are used when computing HC edges for all reanalyses and models. Only monthly-mean zonal wind data are used.

We compare observed and simulated changes in HC width and edges using an optimal fingerprinting technique [*Allen and Stott*, 2003]. In this method, the observed change (**Y**) is regressed onto fingerprint pattern (**X**) using the total least squares method: $\mathbf{Y} = \mathbf{X\beta} + \boldsymbol{\varepsilon}$. Fingerprints are response patterns to a given forcing and estimated from multi-model averages (here 5-year mean time series of HC width and edges obtained from noOZ3, OZ3, or OZ5 multi-model averages). Detection occurs if the 5-95% confidence ranges of the regression coefficient $\boldsymbol{\beta}$ (or scaling factor) lie above zero, implying that the observed change

cannot be explained by the internal variability only (or beyond the uncertainty range of the internal variability). If the uncertainty range of **β** includes unity additionally, the observation is assessed to be consistent with the fingerprint (attribution to the external forcing can be inferred with assumption that there are no other plausible forcings explaining the observed changes). Natural internal variability **ε** is estimated from 376 chunks of non-overlapping CTL5 samples (Table 2) that are divided into two sets. One set is used to estimate the best estimate of the regression coefficient **β** and the other group is used to conduct a standard residual consistency test [*Allen and Tett*, 1999]. According to the residual test, detection results are considered reliable only when observed residual variability is smaller than simulated internal variability.

We use two settings for this analysis: i.e., one-signal and two-signal analyses. In the one-signal analysis, observations are regressed onto each fingerprint separately to look for a significant influence of each forcing. To separate the net influence of stratospheric ozone depletion from the other forcings (mainly GHGs as discussed above), we conduct a two-signal analysis in which observations are regressed simultaneously onto noOZ3 and netOZ3 (estimated from OZ3 minus noOZ3) or onto noOZ3 and netOZ5 (estimated from OZ5 minus noOZ3; note that noOZ5 runs are not available). This provides a way to test the robustness of our results to different model sampling. Although it assumes similar external forcings between CMIP3 and CMIP5 models for the analysis period, this assumption turns out to be reasonably good (see below). In all analyses we use 5-year mean time series so as to remove internal noise at inter-annual time scales. Taking 3-year means does not affect the overall results (not shown). We employ a further dimension reduction using EOF filtering to take account of model skills at simulating internal climate variability, which is assessed by the

standard residual consistency test (see above). It is found that the main results are not affected by the EOF filtering (not shown). As such, we present only the results derived from full dimensional analyses.

3. Results

Figure 1 shows the time series of DJF mean 5-year mean HC width and its southern and northern edges during 1979 to 2009 (30 DJFs). Positive anomalies represent a poleward expansion in each hemisphere. The ENM7 observations show positive trends in Hadley cell width and the southern edge both with a slope of about 0.7° per decade while no trend is seen in the northern edge, consistent with other studies [*Stachnik and Schumacher*, 2011; *Davis and Rosenlof*, 2012].

Model results show that only models with ozone depletion implemented (OZ3 and OZ5) can capture increasing trends in HC width and southern edge as observed, but with smaller amplitudes of 0.2° to 0.3° per decade. The OZ3 and OZ5 results scaled by a factor of 2.5 (dashed lines in Fig. 1) show good agreement with observations. Models without ozone depletion (noOZ3) display negligible trends, indicating a dominant impact of ozone over GHGs. Here it is important to note that the long-term trends of the HC width and edges in the OZ3 and OZ5 runs (and their fingerprints) are quantitatively similar to each other. This suggests that responses of the HC to the external forcings are generally insensitive to different model physics and spatial resolutions if both GHGs increase and stratospheric ozone depletion are reasonably prescribed. This also justifies our assumption that external forcings and their impacts on the HC are similar between the OZ3 and OZ5 runs for the analysis period.

Figure 2 presents optimal detection results based on one-signal detection analyses. It is found that OZ3 and OZ5 are robustly detected for both HC width and southern edge for ENM7 while noOZ3 is not detected. An ozone signal is also detected for individual reanalyses except for MERRA and CSFR which exhibit rather weak trends (see Fig. 4 below). The similar detection results between HC width and southern edge further suggests that the southern edge explains a main portion of the whole HC widening. In contrast, no detection occurs in the northern edges (not shown), which is not surprising as long-term trend in the northern edge is quite weak (Fig. 1).

Results from two-signal analyses are displayed in Fig. 3 for the HC southern edges. Net ozone forcing (netOZ3), which has been estimated from OZ3 minus noOZ3 patterns, is detected from ENM7 and all individual reanalyses except for CSFR. This indicates improved detection through signal separation by two-way regression. Combining with the results from the one-signal analyses (Fig. 2), this suggests that the influence of stratospheric ozone depletion is robustly detected and that ozone has played a dominant role in the HC expansion in austral summer during the past decades. It is also shown that these results are largely insensitive to the use of CMIP5 models (netOZ5) to estimate net ozone fingerprints - The ozone influence is detected from ENM7 and 5 individual reanalyses. As in the one-signal analyses, this represents the insensitiveness of our finding to potential uncertainties arising from using different models.

In both one-signal and two-signal analyses, the best estimates of the scaling factors are much greater than unity with the best estimates being around 2-3 (Figs. 2 and 3), implying that HC expansions in models are underestimated compared to ENM7 observations by the same factor (see scaled time series of HC southern edges from OZ3 and OZ5 in Fig. 1). The

148 cause of this model-observation discrepancy is an unanswered question. Model bias in jet
149 climatology [*Son et al.*, 2010] and a weaker response of modelled convection to surface
150 warming [*Grassi et al.*, 2012] may be in part responsible for the model underestimation.
151 Similar underestimation by the CMIP3 models over the tropics has been found in the trends
152 of zonal-mean precipitation [*Zhang et al.*, 2007; *Noake et al.*, 2012], sea level pressure in DJF
153 [*Gillett and Stott*, 2009], and the hydrological cycle strength inferred from ocean salinity
154 change [*Durack et al.*, 2012].

155 In order to examine the possible influence of model performance, we test the sensitivity of
156 our detection results to the use of selected models that can reasonably simulate the
157 climatology of the HC southern edges. It requires the model climatology to be placed within
158 ±5% of the ENM7 (33.9-37.4°S) as indicated in Fig. 4. By doing this, about half the models
159 are selected (3, 4, and 15 models for noOZ3, OZ3, and OZ5 respectively, see Table 2 for the
160 list). Single-signal analyses with these selected models show essentially the same results to
161 those from the full model case (not shown). Two-signal analyses are also unaffected by the
162 different model sampling (Fig. 5). This provides robustness of our findings to the model
163 performance (cf. Santer et al. 2009). It is also consistent with weak intra-ensemble
164 relationships between means and trends of the HC southern edge location (correlation
165 coefficients r = 0.26, 0.09, and -0.06 for noOZ3, OZ3, and OZ5). Reanalyses show a higher
166 correlation (r = 0.54), but this is not statistically significant given 7 samples (Fig. 4).

167 We have repeated our detection analyses of the SH HC changes for other seasons during
168 1979-2008 and found neither the OZ nor the noOZ signal to be as robustly detected as in DJF
169 (not shown). When comparing trends of the HC southern edges from reanalyses and CMIP3
170 and CMIP5 simulations (see scatter plots in Fig. 6), model-simulated trends are found to be

too weak compared to the observations, particularly in austral autumn (March to May, MAM). This might represent missing external forcings in the model simulations and/or a larger influence of natural climate variability on the observed trend. For the latter, *Grassi et al.*, [2012] has suggested a possible effect of the Pacific decadal oscillation on HC expansion during MAM and September-November (SON). The SH HC changes in austral winter (July-August, JJA) and spring (SON) are characterized by much weaker trends in both models and reanalyses, also with larger difference among reanalyses (Fig. 6). The intra-ensemble relationships between means and trends of the HC southern edge location are low in the models in all seasons. Interestingly, reanalyses show statistically significant correlation coefficients in MAM (0.84) and SON (0.94), but this is determined by two outlier reanalyses (JRA25 and MERRA) and not supported by models, questioning reliability. We have also conducted detection analyses for the Northern Hemisphere (NH) HC changes and obtained no detection of OZ and noOZ signals across all seasons (not shown). It is confirmed that CMIP3 and CMIP5 models cannot reproduce the observed NH-summer HC expansion. *Allen et al.*, [2012] has shown that black carbon and tropospheric ozone can induce northern tropical expansion in boreal summer. Therefore, clear isolation of a human influence on tropical expansion other than stratospheric ozone depletion requires further investigation.

4. Conclusions

We compare multiple reanalyses and multiple climate model simulations in terms of long-term changes in HC width and northern and southern edges during the past three decades using an optimal fingerprinting technique. Results show that anthropogenic stratospheric ozone depletion has significantly contributed to the observed HC widening. It is also found

194 that HC widening has occurred mainly in its southern edge in austral summer and that the
195 ozone influence is well separable from other external forcings including GHG increase. The
196 CMIP3 and CMIP5 models that consider ozone depletion deliver good agreement, indicating
197 the robustness of model responses to model structural uncertainty. Our results re-confirm
198 that stratospheric ozone has been a main driver of observed changes in the Southern
199 Hemisphere [Son et al., 2009, 2010; *McLandress et al.*, 2011; *Polvani et al.*, 2011b].
200 Nevertheless, both CMIP3 and CMIP5 models underestimate the observed changes by a
201 factor of 2-3. What causes the model-observation discrepancy is an open question.

202 This study utilizes various CMIP3 and CMIP5 models that have different model physics,
203 resolution and external forcings. Since models in noOZ3 group and those in OZ3 group are
204 different in many other aspects, the difference between noOZ3 and OZ3 model results is not
205 necessarily due to stratospheric ozone depletion alone. However, recent studies using
206 model sensitivity test have shown that multi-model means of noOZ3 and OZ3 runs well
207 represent stratospheric-ozone related climate change in the SH [*McLandress et al.*, 2011;
208 *Polvani et al.*, 2011b]. This allows us to attribute SH HC expansion to stratospheric ozone
209 depletion and GHGs increase separately in this study.

210 Stratospheric ozone is anticipated to recover by the mid-21st century [*Eyring et al.*, 2007],
211 and this would affect SH climate in the opposite way to GHGs increase [*Son et al.*, 2009;
212 *Polvani et al.*, 2011a]. The physical mechanism(s) how stratospheric ozone chances
213 influence the tropospheric circulation such as the HC, however, is still unclear [*Hu et al.*,
214 2011], which may involve stratosphere-troposphere coupling [*Polvani and Kushner*, 2002],
215 static stability [*Frierson*, 2006; *Lu et al.*, 2007], and baroclinic eddies [*Chen et al.*, 2008]. To
216 better understand the HC change in the past and future climate, it reserves further analyses.

Acknowledgements. We thank Ji Wook Hwang for his assistance in processing model data and Betrand Timbal, Kevin Grise, Bin Yu, and Ian Watterson their useful comments. We acknowledge the World Climate Research Programme's Working Group on Coupled Modelling, which is responsible for Coupled Model Intercomparison Project (CMIP), and we thank the climate modeling groups (listed in Table 2 of this paper) for producing and making available their model output. For CMIP the U.S. Department of Energy's Program for Climate Model Diagnosis and Intercomparison provides coordinating support and led development of software infrastructure in partnership with the Global Organization for Earth System Science Portals. This study is partly supported by the Goyder Institute for Water Research.

References

Allen, M. R., and S. F. B. Tett (1999), Checking for model consistency in optimal fingerprinting, *Clim. Dyn.*, *15*, 419-434.

Allen, M. R., and P. A. Stott (2003), Estimating signal amplitudes in optimal fingerprinting, part I: theory, *Clim. Dyn.*, *21*, 477-491.

Allen, R. J., S. C. Sherwood, J. R. Norris, and C. S. Zender (2012), Recent Northern Hemisphere tropical expansion primarily driven by black carbon and tropospheric ozone, *Nature*, *485*, 350-354.

237 Chen, G., J. Lu, and D. M. W. Frierson (2008), Phase Speed Spectra and the Latitude of
238 Surface Westerlies: Interannual Variability and Global Warming Trend, *J. Clim.*, *21*, 5942-
239 5959.

240 Davis, S. M., and K. H. Rosenlof (2012), A Multidiagnostic Intercomparison of Tropical-Width
241 Time Series Using Reanalyses and Satellite Observations, *J. Clim.*, *25*, 1061-1078.

242 Durack, P. J., S. E. Wijffels, and R. J. Matear (2012), Ocean Salinities Reveal Strong Global
243 Water Cycle Intensification During 1950 to 2000, *Science*, *336*, 455-458.

244 Eyring, V., et al. (2007), Multimodel projec L24816, doi:10.1029/2006GL027504.
245 tions of stratospheric ozone in the 21st century, *J. Geophys. Res., 112,* D16303,
246 doi:10.1029/2006JD008332.

247 Frierson, D. M. W. (2006), Robust increases in midlatitude static stability in simulations of
248 global warming, *Geophys. Res. Lett.*, *33,* L24816, doi:10.1029/2006GL027504.

249 Gillett, N. P., and P. A. Stott (2009), Attribution of anthropogenic influence on seasonal sea
250 level pressure, *Geophys. Res. Lett., 36,* L23709, doi:10.1029/2009GL041269.

251 Grassi, B., G. Redaelli, P. Osvaldo Canziani, and G. Visconti (2012), Effects of the PDO Phase
252 on the Tropical Belt Width, *J. Clim.*, *25*, 3282-3290.

253 Hegerl, G. C., and F. W. Zwiers (2011) Use of models in detection and attribution of climate
254 change. *WIRE Climate Change, 2,* 570-591, doi:10.1002/wcc.121.

255 Hu, Y., and Q. Fu (2007), Observed poleward expansion of the Hadley circulation since 1979,
256 *Atmos. Chem. Physics*, *7*, 5229-5236.

257 Hu, Y., C. Zhou, and J. Liu (2011), Observational Evidence for Poleward Expansion of the
258 Hadley Circulation, *Adv. Atmos. Sci.*, *28*, 33-44.

259 Johanson, C. M., and Q. Fu (2009), Hadley cell widening: Model simulations versus
260 observations, *J. Clim.*, *22*, 2713-2725.

261 Lu, J., G. A. Vecchi, and T. Reichler (2007), Expansion of the Hadley cell under global
262 warming, *Geophys. Res. Lett., 34, L06805, doi:10.1029/2006GL028443.*

263 Lu, J., C. Deser, and T. Reichler (2009), Cause of the widening of the tropical belt since 1958,
264 *Geophys. Res. Lett., 36,* L03803, doi:10.1029/2008GL036076.

265 McLandress, C., T. G. Shepherd, J. F. Scinocca, D. A. Plummer, M. Sigmond, A. I. Jonsson, and
266 M. C. Reader (2011), Separating the dynamical effects of climate change and ozone
267 depletion. Part II southern hemisphere troposphere, *J. Clim.*, *24*, 1850-1868.

268 Meehl, G. A., C. Covey, T. Delworth, M. Latif, B. McAvaney, J. F. B. Mitchell, R. J. Stouffer,
269 and K. E. Taylor (2007), The WCRP CMIP3 multimodel dataset - A new era in climate change
270 research, *Bull. Amer. Meteor. Soc.*, *88*, 1383-1394.

271 Ming, Y., and V. Ramaswamy (2011), A model investigation of aerosol-induced changes in
272 tropical circulation, *J. Clim.*, *24*, 5125-5133.

273 Noake, K., D. Polson, G. Hegerl, and X. Zhang (2012), Changes in seasonal land precipitation
274 during the latter twentieth-century, *Geophys. Res. Lett.*, *39*, L03706,
275 doi:10.1029/2011GL050405.

276 Polvani, L. M., and P. J. Kushner (2002), Tropospheric response to stratospheric
277 perturbations in a relatively simple general circulation model, *Geophy. Res. Lett.*, *29(7),* 1114,
278 doi:10.1029/2001GL014284.

279 Polvani, L. M., M. Previdi, and C. Deser (2011a), Large cancellation, due to ozone recovery,
280 of future Southern Hemisphere atmospheric circulation trends, *Geophys. Res. Lett., 38,*
281 L04707, doi:10.1029/2011GL046712.

282 Polvani, L. M., D. W. Waugh, G. J. P. Correa, and S.-W. Son (2011b), Stratospheric Ozone
283 Depletion: The Main Driver of Twentieth-Century Atmospheric Circulation Changes in the
284 Southern Hemisphere, *J. Clim.*, *24*, 795-812.

285 Santer, B. D., et al. (2009), Incorporating model quality information in climate change
286 detection and attribution studies, *Proc. Natl. Acad. Sci. USA*, *106*, 14778-14783.

287 Seidel, D. J., Q. Fu, W. J. Randel, and T. J. Reichler (2008), Widening of the tropical belt in a
288 changing climate, *Nature Geoscience*, *1*, 21-24.

289 Son, S., N. F. Tandon, L. M. Polvani, D. W. Waugh, and S. W. Son (2009), Ozone hole and
290 Southern Hemisphere climate change, *Geophys. Res. Lett.*, *36*, L15705,
291 doi:10.1029/2009GL038671.

292 Son, S. W., et al. (2010), Impact of stratospheric ozone on Southern Hemisphere circulation
293 change: A multimodel assessment, *J. Geophys. Res., 115,* D00M07,
294 doi:10.1029/2010JD014271.

295 Stachnik, J. P., and C. Schumacher (2011), A comparison of the Hadley circulation in modern
296 reanalyses, *J. Geophys. Res., 116,* D22102, doi:10.1029/2011JD016677.

297 Taylor, K. E., R. J. Stouffer, G. A. Meehl (2012) An Overview of CMIP5 and the experiment
298 design. *Bull. Amer. Meteor. Soc.*, 93, 485-498.

299 Zhang, X. B., F. W. Zwiers, G. C. Hegerl, F. H. Lambert, N. P. Gillett, S. Solomon, P. A. Stott,
300 and T. Nozawa (2007), Detection of human influence on twentieth-century precipitation
301 trends, *Nature*, *448*, 461-465.

302

303

304 **Table 1.** List of 7 reanalyses used in this study. A common analysis period of 1979-2009 has

305 been employed to construct the ensemble mean (ENM7).

Name	Source	Data period (DJF)	Horizontal Resolution
ERA-Interim	ECMWF	1979-2010	1.5° × 1.5°
JRA	JMA	1979-2010	1.25° × 1.25°
MERRA	NASA	1979-2010	1.25° × 1.25°
NCEP1	NCEP/NCAR	1958-2010	2.5° × 2.5°
NCEP2	NCEP/DOE	1979-2010	2.5° × 2.5°
20CR	NOAA/CIRES	1871-2010	2.0° × 2.0°
CFSR	NASA	1979-2009	0.5° × 0.5°

306

307 **Table 2.** List of CMIP3 and CMIP5 coupled climate model simulations used in this study.
308 Values in parentheses in noOZ3, OZ3 and OZ5 represent the number of ensemble runs of
309 each model. Those in CTL5 denote the number of non-overlapping 50-year chunks for
310 CMIP5 preindustrial control runs. Refer to text for details on how model groups of noOZ3,
311 OZ3, and OZ5 are defined and how they are extended up to 2009. Asterisk represents
312 models with high skill at simulating the climatology of the HC's southern edge. See text for
313 details.

Group	noOZ3	OZ3	OZ5	CTL5
Model	BCCR-BCM2(1)* CGCM3.1-T47(5) CGCM3.1-T63(1) CNRM-CM3(1)* GISS-AOM(2) FGOALS-G1.0(3) INM-CM3(1)* IPSL-CM4(1)	CSIRO-Mk3.0(1)* CSIRO-Mk3.5(1) GFDL-CM2.0(1) GFDL-CM2.1(1)* INGV-SXG(1) MIROC3.2-hi(1) MIROC3.2-med(3) MPI-ECHAM5(4)* CCSM3(7)*	ACCESS1.3(1)* BCC-CSM1.1(1)* BNU-ESM(1) CanCM4(10)* CanESM2(5)* CCSM4(5) CMCC-CM(1) CNRM-CM5(1)* FGOALS-g2(1) FGOALS-s2(1) GFDL-CM3(1)* GFDL-ESM2G(1)* GFDL-ESM2M(1)* GISS-E2-R(15) HadCM3(4) HadGEM2-AO(1)* HadGEM2-CC(1) HadGEM2-ES(4) INM-CM4(1)* IPSL-CM5A-LR(4) IPSL-CM5A-MR(1) MIROC4h(3)* MIROC5(3)* MIROC-ESM(1) MIROC-ESM-CHEM(1) MPI-ESM-LR(3)* MPI-ESM-MR(1) MRI-CGCM3(1)* NorESM1-M(1)* NorESM1-ME(1)	ACCESS1.3(4) BCC-CSM1.1(10) BNU-ESM(10) CanESM2(20) CCSM4(10) CESM1-CAM5(6) CESM1-FASTCHEM(4) CESM-WACCM(4) CMCC-CM(6) CNRM-CM5(14) CSIRO-Mk3-6-0(10) FGOALS-g2(14) FGOALS-s2(6) FIO-ESM(16) GFDL-CM3(10) GFDL-ESM2G(2) GFDL-ESM2M(10) GISS-E2-H(18) GISS-E2-R(52) INM-CM4(10) IPSL-CM5A-LR(20) IPSL-CM5A-MR(6) MIROC4h(2) MIROC5(12) MIROC-ESM(10) MIROC-ESM-CHEM(4) MPI-ESM-LR(20) MPI-ESM-MR(20) MPI-ESM-P(22) MRI-CGCM3(10) NorESM1-M(10) NorESM1-ME(4)
Counts	8 models (15 runs)	9 models (20 runs)	30 models (76 runs)	32 models (376 chunks)

314

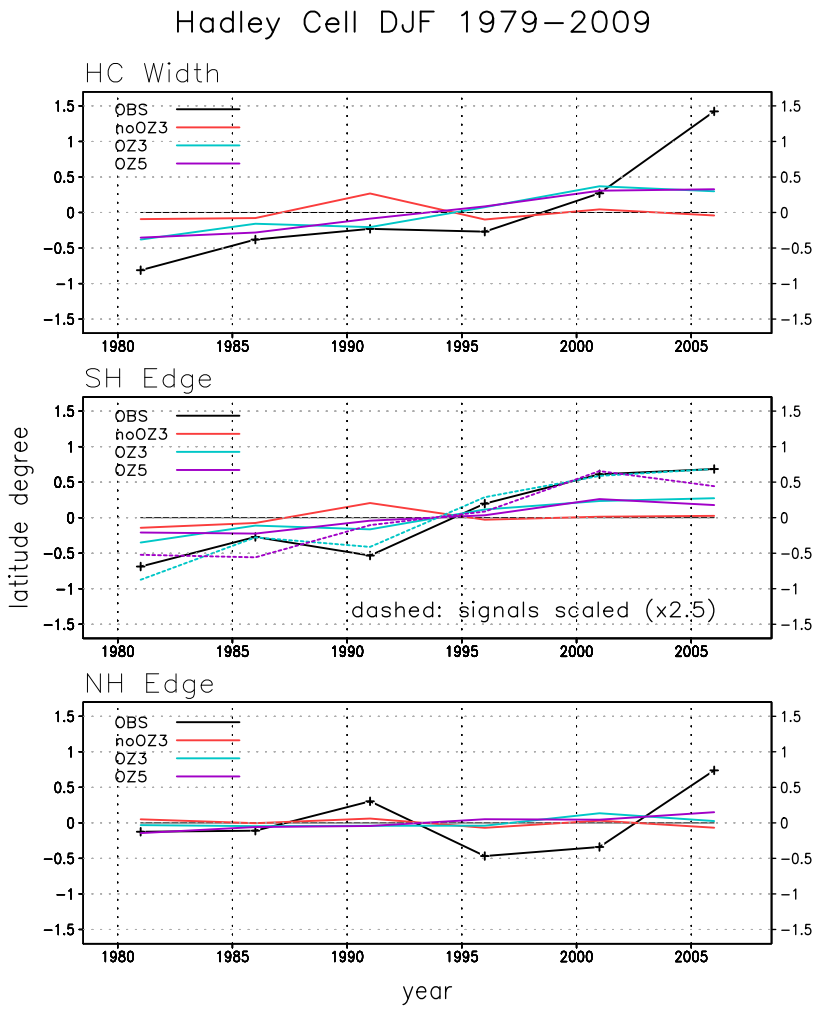

315

316 **Fig. 1.** Time series of 5-year mean DJF Hadley cell width (top), southern edge (middle), and
317 northern edge anomalies (bottom) for 1979-2009 (30 DJFs). Observations show the
318 ensemble average of seven reanalyses (ENM7). Simulated results are multi-model averages
319 from CMIP3 models without and with ozone depletion (noOZ3 and OZ3 respectively) and
320 CMIP5 models (OZ5). Anomalies are relative to each time mean and units are latitude
321 degree. X-axis represents center years of 5-year intervals. Refer to Tables 1 and 2 for the list
322 of reanalyses and model runs. Dashed lines in middle panel represent scaled OZ3 and OZ5
323 results multiplied by 2.5.

324

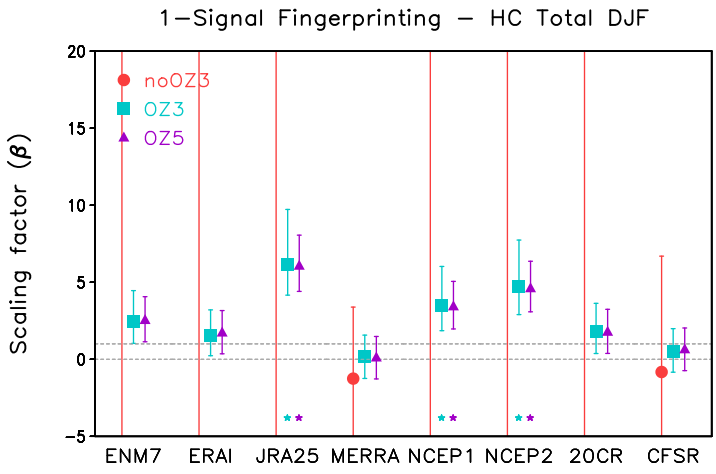

325

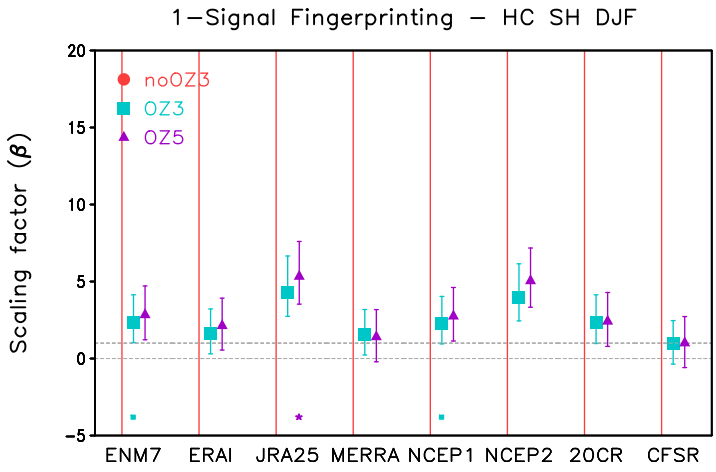

326

327 **Fig. 2.** Results from one-signal detection analyses for DJF Hadley cell width (upper) and
328 Southern edge (lower) from 1979-2009 when using the reanalysis ensemble mean (ENM7)
329 and individual reanalyses as observations (see Table 1). Observations are regressed
330 separately onto multi-model simulated fingerprints of noOZ3, OZ3, and OZ5, which is
331 conducted in the full space of 5-dimensional analysis vector (demeaned 5-year mean series).
332 Marks depict best estimates of the regression coefficients (or scaling factors **β**) and error
333 bars represent 5-95% uncertainty ranges. An error bar without a data point represents
334 unbounded uncertainty in estimating **β** ranges. Asterisk [square] indicates failure of the
335 residual consistency test [*Allen and Tett*, 1999] because modelled variability is too small [too
336 large]. Dashed lines denote zero and unity of **β**.

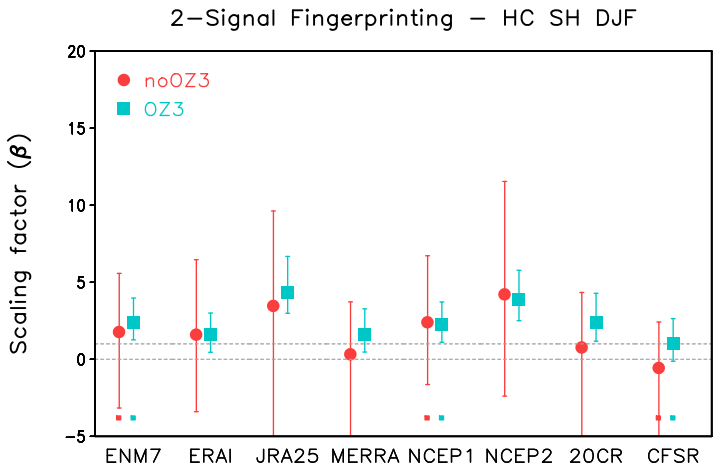

337

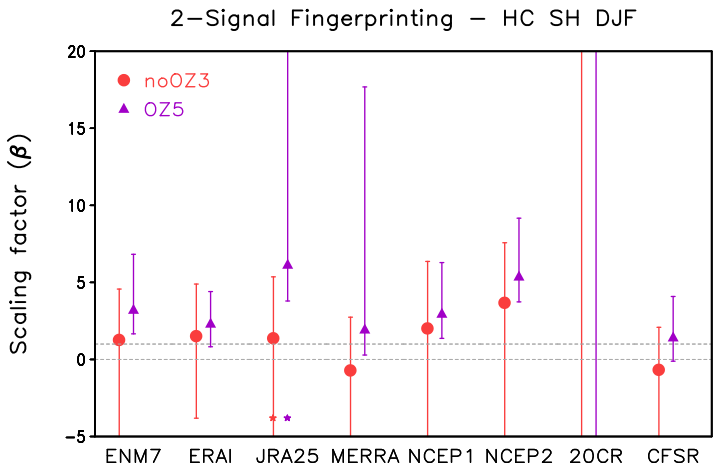

338

339 **Fig. 3.** Same as Fig. 2 but for two-signal detection analyses for DJF Hadley cell southern edge.
340 Observations of ENM7 are regressed simultaneously onto noOZ3 and netOZ3 (estimated
341 from OZ3 – noOZ3, upper) or onto noOZ3 and netOZ5 (estimated from OZ5 – noOZ3,
342 bottom) fingerprints.

343

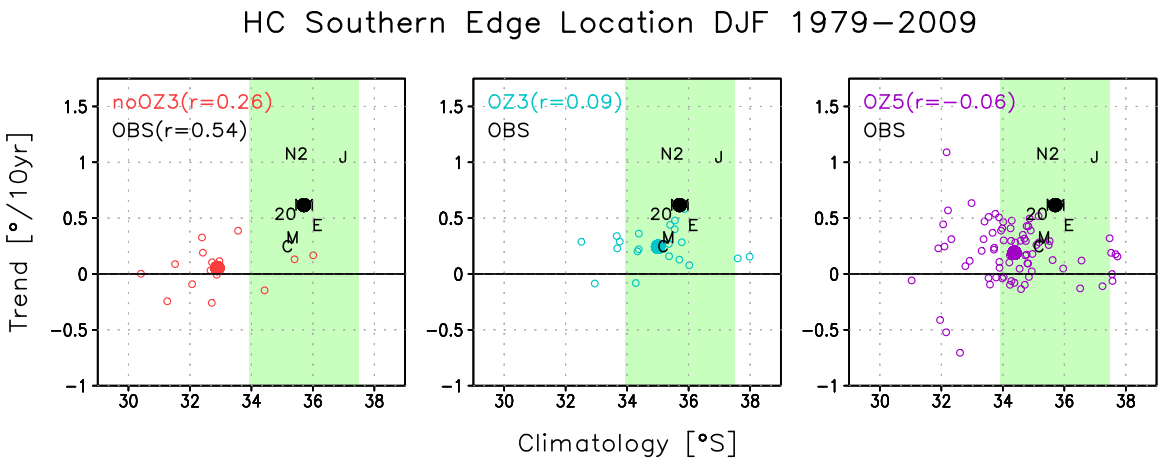

344

345

346 **Fig. 4.** Scatter plots between means (x-axis) and trends (y-axis) of the DJF HC southern edge
347 latitude for noOZ3, OZ3, and OZ5 simulations and ENM7 reanalyses (OBS – E, J, M, N1, N2,
348 20, and C denote ERA-Interim, JRA, MERRA, NCEP1, NCEP2, 20CR, and CFSR respectively).
349 Open circles represent values from individual ensemble members and closed circles are
350 multi-model or multi-reanalysis ensemble means. Correlation coefficients (r) between the
351 mean and trend across ensemble members are provided in parentheses. The green area
352 depicts ±5% ranges of the ENM7 mean of the southern edge location.

353

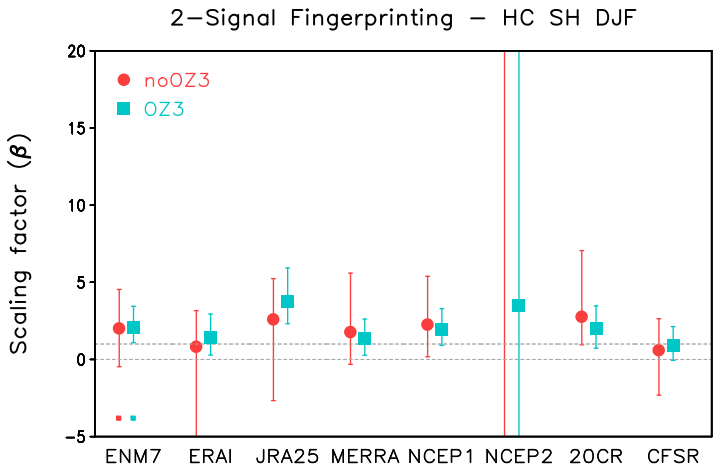

354

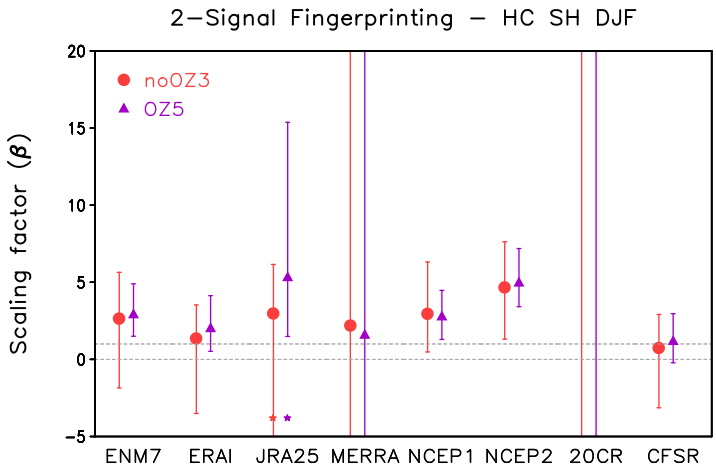

355

356 **Fig. 5.** Same as Fig. 3 except for using selected models that can simulate the observed
357 climatology of the HC southern edge latitudes (models within the green area in Fig. 4). See
358 text for more details on model selection.

359

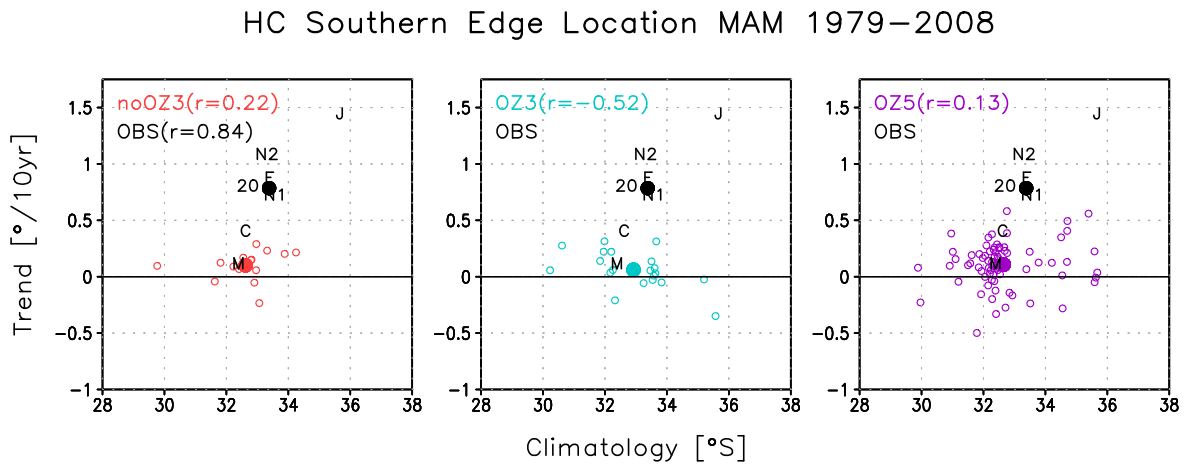

360

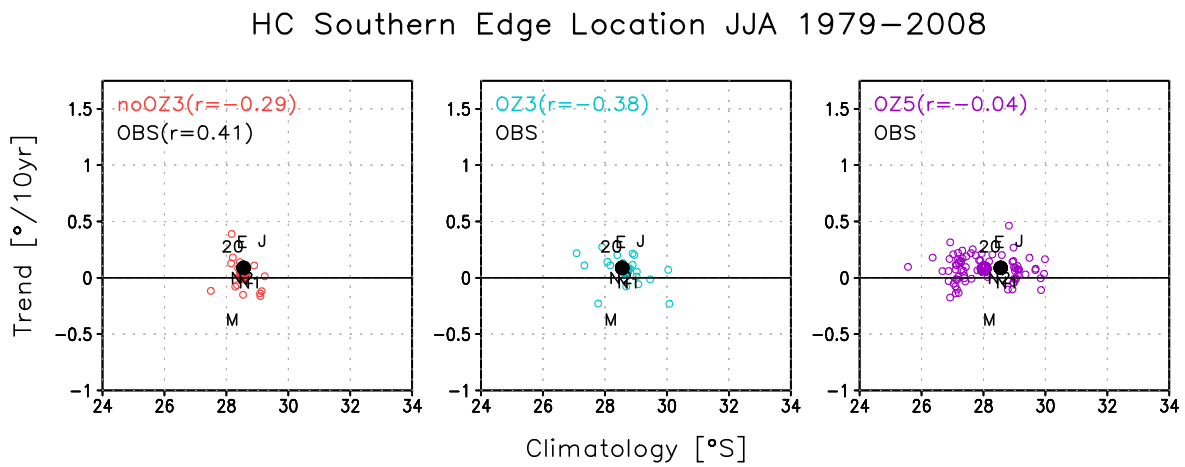

361

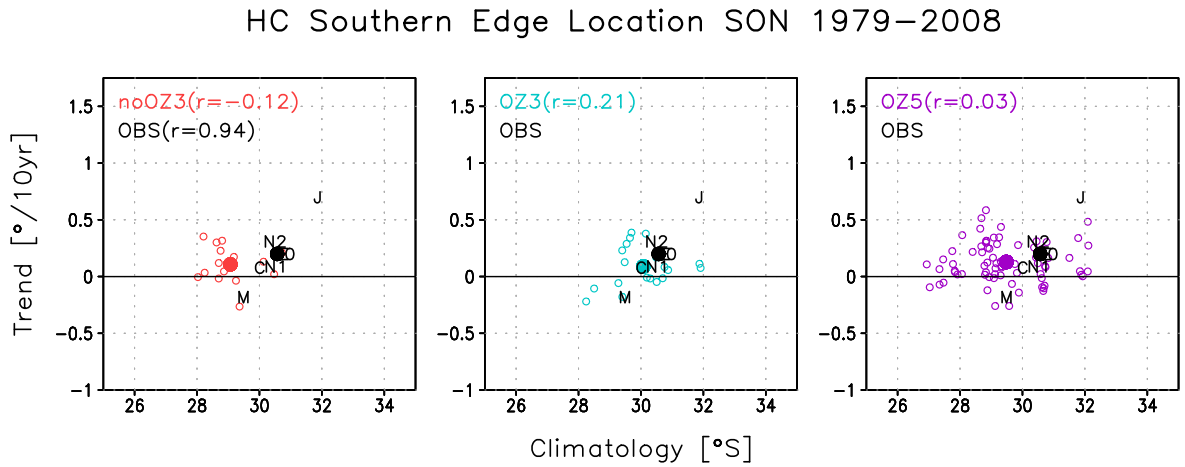

362

363 **Fig. 6.** Same as Fig. 4 except for MAM, JJA, and SON during 1979-2008. Note different

364 latitude ranges (x-axis) among seasons. CSFR is excluded in JJA due to missing HCs.